A modified mixed-mode Timoshenko-based peridynamics model considering shear deformation

Victor Bautista, Behnam Shahbazian, Mirmilad Mirsayar*

Department of Aerospace, Physics, and Space Sciences, Florida Institute of Technology, Melbourne, Florida 32901, USA

Abstract

The original two-dimensional bond-based peridynamic (BBPD) framework, which only considers the pairwise forces (compression and tension) between two material points, is extended by incorporating the effect of shear deformation in the calculations and its influence on the failure of the bonds. To this end, each bond is considered as a short Timoshenko beam, and by doing so, the traditional BBPD is enhanced into a more comprehensive model known as multi-polar peridynamic (MPPD). The proposed novel approach explicitly considers the shear influence factor used in Timoshenko beams and introduces a strain-based shear deformation failure criterion. The model is then validated against two benchmark experimental tests (i.e., a standard pure mode I edge crack, and a Kalthoff-Winkler configuration) reported in the literature under in-plane dynamic loading and plane stress conditions. In most cases, the developed model is shown to be more accurate in predicting the crack paths obtained from the experimental results when compared to other theoretical methods delineated in the literature. Furthermore, a noticeable change in crack branching and crack path is observed in a study on the effects of Poisson's ratio and the loading rate. This investigation also demonstrated that the proposed MPPD model can accommodate materials with Poisson's ratios up to 1/3, expanding the range beyond the traditional BBPD limitations.

Keywords: dynamic brittle fracture; computational fracture mechanics; crack branching; peridynamics; Timoshenko beam theory; mixed-mode I/II loading

Nomenclature

$\boldsymbol{b}$	External body force density field.
BBPD	Bond based peridynamics.
c	Bond axial micromodulus.
CM	Continuum mechanics.
dV_x	Particle's infinitesimal volume.
E	Young's modulus.
$\boldsymbol{f}$	Pair-wise force function.
G_0	Fracture energy.
h	Thickness.
H_x	Particle's neighborhood or horizon.
J_ρ	Specific polar mass moment of inertia.
k	Bulk modulus.
$\boldsymbol{m}$	Pair-wise moment function.
MPPD	Multipolar peridynamics.
$\boldsymbol{n}$	External body moment density field.
NO-SBPD	Non-ordinary state-based peridynamics.
O-SBPD	Ordinary state-based peridynamics.
PD	Peridynamics.
s	Bond stretch.
s_0	Critical bond stretch.
SBPD	State-based peridynamics.
t_n, t_{n-1}	Time in the current and the previous time step.
$\boldsymbol{u}, \dot{\boldsymbol{u}}, \ddot{\boldsymbol{u}}$	Particle's displacement, velocity, and acceleration vector.
V_{tip}	Crack tip velocity.
w	Micropotential.
W	Strain energy density.
$\boldsymbol{x}$	Particle's coordinates.
$\boldsymbol{x'}$	Neighbor's coordinates.
$\boldsymbol{x}_n, \boldsymbol{x}_{n-1}$	Crack tip position in the current and the previous time step.
XFEM	Extended finite element method.
γ	Bond shear deformation.
γ_0	Critical bond shear deformation.
δ	Radius of the horizon.
Δt	Time step.
$\boldsymbol{\eta}$	Relative displacement of two particles.
$\theta, \dot{\theta}, \ddot{\theta}$	Angular orientation, speed, and acceleration.
κ	Bond shear micromodulus.
μ	Damage history-dependent scalar value function.
ν	Poisson's ratio.
$\boldsymbol{\xi}$	Relative position of two particles in the reference configuration.
ρ	Material density.
φ	Damage parameter.
φ_x	Shear influence factor.

1. Introduction

Dynamic fracture mechanics, a discipline focusing on the behavior of rapidly propagating cracks, has been an evolving topic of research due to its importance in fields ranging from aerospace engineering to geophysics [1-5]. The complexity of dynamic fractures, characterized by rapid crack propagation, stress wave interaction, and branching, leads to unique challenges that traditional analytical methods tend to neglect [6-12]. This has required the development of robust numerical methods capable of simulating such phenomena with greater accuracy.

Even though traditional methods are effective in certain scenarios such as quasi-static loading, they often fall short of accurately capturing the details of dynamic fracture processes (i.e., the prediction of crack initiation angle and crack path) [2, 14-16]. This gap led to the evolution of advanced computational techniques such as atomistic models [17, 18], lattice models [19], continuum-based models (FEM and XFEM) [20-27], and phase field models [28, 29, 30]. In the case of atomistic models, as the name implies, it would require recreating an entire structure to the atomic level in order to predict the interaction between the stress waves and the boundaries, which is computationally unfeasible [17, 18]. Moreover, these models have been shown to estimate crack branching angles much greater than those seen experimentally or to those estimated by other models [31]. Lattice models tend to predict crack propagation speeds significantly larger than theoretically permissible or seen experimentally [19]. Both continuum-based and phase field models show better performance and accuracy than the latter two. Nevertheless, some major drawbacks arise in complex dynamic scenarios. In the continuum-based approaches (i.e. FEM and XFEM models) additional failure criteria are required. For FEM methods when such failure criteria are met, the crack propagates by either erasing elements, or a cohesive model is applied to separate the pertinent nodes. Hence, in both cases, the crack path will be strongly influenced by the mesh [21, 22, 23]. The XFEM method permits cracks to propagate through elements, however, constant crack tip tracking and bifurcation criteria are required to estimate the crack path, leading to higher computational expenses than its predecessor [20]. Most importantly, the crack propagation speeds differ significantly from those observed experimentally, unless the material's fracture energy is considerably modified [27]. Phase field models use an energy minimization approach based on elastic and fracture energy through a coupled system of equations considering classical elasticity and a continuous damage model [28, 29, 30]. Nonetheless, phase field theory does not guarantee

to find the lowest energy solution due to the nonconvexity of the energy functional, possibly converging in a local minimum, and predicting erroneous crack paths [31, 32, 33].

In recent years, peridynamics, a nonlocal reformulation of classical continuum mechanics developed by S.A. Silling in the early 2000s, which has been a significant contribution to the field [34-40]. With its integro-differential equation approach, peridynamics offers a more direct way of simulating the discontinuities inherent in fracture mechanics (i.e., cracks). Unlike classical continuum mechanics, which relies on partial differential equations and spatial derivatives, peridynamics employs integral equations, thereby enabling a more natural treatment of discontinuities [34]. This feature makes peridynamics particularly suitable for modeling complex crack initiation and propagation scenarios in dynamic fracture mechanics. It offers valuable insights into the mechanics behind crack branching and path instability by effectively modeling how stress wave propagation influences crack initiation and growth [41-44].

The original Bond-Based Peridynamic (BBPD) theory, the first and simplest variant of the peridynamic theory, considers interactions between material points to be linear pairwise forces, making it computationally efficient [45, 46]. However, BBPD has been limited by its inability to accurately model materials with varying Poisson's ratios, as it is fixed to 1/3 in 2D and 1/4 in 3D [45, 46]. To circumvent this limitation, several modifications to the BBPD model have been proposed to incorporate more complex material behaviors and interactions. For instance, Silling later introduced other numerical methods like Ordinary State-Based Peridynamic (O-SBPD) or Non-Ordinary State-Based Peridynamics (NO-SBPD) [49-52]. Although the mentioned approaches are capable of solving the fixed Poisson’s ratio restriction seen in bond-based peridynamics, these numerical methods are significantly more computationally expensive than the original BBPD [40, 45, 53-56]. Consequently, there has been a focus on creating improved versions of bond-based peridynamics known as multipolar peridynamics (MPPD). Such models moved away from the idea of treating the bonds as purely linear springs by accounting for the effects of shear deformation and rotation in the simulation [46, 57-59]. Some researchers, such as Gerstle [60, 61], have treated these bonds as Euler-Bernoulli beams. By doing so, they not only vanquished the Poisson’s ration limitation in the original BBPD but also achieved a more accurate prediction of mixed-mode dynamics crack propagation [40, 60, 61].

The drawback of the Euler-Bernoulli beam theory is that it assumes that the cross-section of the beam is always perpendicular to the longitudinal axis and neglects the effect of shear deformation, which leads to artificially stiffening effects [62]. This stiffening effect and inaccuracy in predicting beam deformation is even more prominent in short beams, thereby making it unsuitable for such conditions. A recent approach to increase the accuracy of the multipolar peridynamics in predicting stress wave propagation, crack initiation, and crack path, is to use a more sophisticated theory, such as treating the bonds as Timoshenko beams. The Timoshenko beam theory, developed in the 20^{th} century by Stephen Timoshenko and Paul Ehrenfest, allows rotation of the beam's cross-section with respect to the bending line and includes the effect of shear deformation, allowing it to predict the deformation of stubby beams with much greater accuracy [63]. Therefore, given that peridynamic bonds have varying lengths within the peridynamic horizon, utilizing Timoshenko beam theory over Euler-Bernoulli beam theory ensures a more accurate approximation of the behavior of materials under complex loading conditions.

Incorporating the Timoshenko beam theory into the BBPD framework represents a significant advancement in the area of dynamic fracture mechanics, however, only modified versions of this theory have been applied to peridynamics [64, 65]. The Timoshenko beam theory, known for its ability to account for both bending and shear effects in beam deformation, offers a more realistic representation of beam/bond behavior, particularly in cases where shear deformation is non-negligible [66, 67, 68]. Integrating this theory into the BBPD model aims to overcome the existing limitations regarding Poisson's ratio and enhance the capability of BBPD in accurately simulating in-plane mixed-mode fractures. This integration not only addresses a long-standing limitation in the BBPD theory but also broadens the scope of its application in computational fracture mechanics [69].

The current work focuses on this integration, exploring the potential of the enhanced BBPD model (Timoshenko MPPD) in providing more accurate and comprehensive tools for the simulation of dynamic fractures. This advancement is expected to have significant implications in a wide range of engineering applications where understanding and predicting fracture behavior under dynamic loading conditions is vital.

2. Theoretical framework

2.1. Bond-Based Peridynamics

The classical bond-based peridynamics can be thought of as a nonlocal version of continuum mechanics as expressed by Silling [34]. In the nonlocal method, a particle $\boldsymbol{x}$ interacts with all other particles $\boldsymbol{x}'$ within a neighborhood or horizon $\boldsymbol{H_x}$, of radius δ, through the so-called "bonds", thus the name *bond-based peridynamics.* The acceleration of a particle $\boldsymbol{x}$ can be found by the following integral equation, known as the peridynamic equation of motion:

$$\rho\ddot{\boldsymbol{u}}(\boldsymbol{x},t) = \int_{H_x} \boldsymbol{f}(\boldsymbol{u}(\boldsymbol{x}',t) - \boldsymbol{u}(\boldsymbol{x},t), \boldsymbol{x}' - \boldsymbol{x}) dV_{\boldsymbol{x}'} + \boldsymbol{b}(\boldsymbol{x},t) \ , \tag{1}$$

where ρ is the density of the material, $\ddot{\boldsymbol{u}}$ is the acceleration vector of particle $\boldsymbol{x}$, $\boldsymbol{u}$ is the displacement vector field, $\boldsymbol{b}$ is an external body force density field, $dV_{x'}$ is the differential volume element at the material point $\boldsymbol{x}'$, and $\boldsymbol{f}$ is a pairwise force vector in units of force per unit volume squared. Fig. 1 depicts the undeformed and deformed configurations of two neighboring peridynamic nodes.

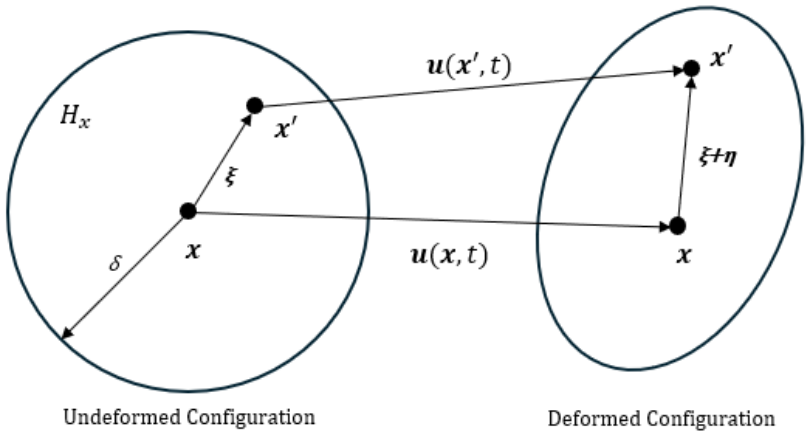

Fig. 1. Undeformed and deformed configuration of peridynamic bonds and horizon.

In peridynamic notation, the relative position of two particles in the reference configuration is:

$$\boldsymbol{\xi} = \boldsymbol{x}' - \boldsymbol{x} \ , \tag{2}$$

and their relative displacement is denoted as:

$$\boldsymbol{\eta} = \boldsymbol{u}(\boldsymbol{x}',t) - \boldsymbol{u}(\boldsymbol{x},t) \ . \tag{3}$$

For a microelastic material, the pairwise force function derives from the change in micropotential energy with the change in the deformation of the bond as:

$$f(\boldsymbol{\eta}, \boldsymbol{\xi}) = \frac{\partial w}{\partial \boldsymbol{\eta}}(\boldsymbol{\eta}, \boldsymbol{\xi}) \qquad \forall\, \boldsymbol{\xi}, \boldsymbol{\eta} \quad . \tag{4}$$

The *linear microelastic potential* can be obtained from the following expression [34, 37]:

$$w = \frac{cs^2|\boldsymbol{\xi}|}{2} \quad , \tag{5}$$

where c is the bond elastic stiffness in units of force per unit volume squared, and s is the stretch of a bond, defined very similarly to strain in one dimension as follows:

$$\boldsymbol{s} = \frac{|\boldsymbol{\eta} + \boldsymbol{\xi}| - |\boldsymbol{\xi}|}{|\boldsymbol{\xi}|} = \frac{y - |\boldsymbol{\xi}|}{|\boldsymbol{\xi}|} \quad . \tag{6}$$

Then, the strain energy density at any point in the material is computed by integrating the micropotential energy over the node's neighborhood:

$$W_{PD} = \frac{1}{2}\int_{H_x} w(\boldsymbol{\eta}, \boldsymbol{\xi}) dV_{\xi} \quad , \tag{7}$$

and notice the 1/2 factor as each endpoint of the bond takes half of the strain energy [34, 37]. BBPD introduces the concept of failure and crack propagation by allowing the bonds to break after a critical stretch limit, s_0, is reached, and making it incapable of bearing any force from that instance, leading to the model being history dependent [34, 37, 43]. Thus, failure is considered in the pairwise force function by recasting the equation as follows:

$$f(y(t), \boldsymbol{\xi}) = g\big(s(t, \boldsymbol{\xi})\big)\mu(t, \boldsymbol{\xi}) \quad , \tag{8}$$

where g is a linear scalar-valued function,

$$g(s) = cs \quad \forall s \quad , \tag{9}$$

and μ is a history-dependent scalar-valued function whose value is equal to unity if the bond is "healthy" (it hasn't surpassed the critical bond stretch), or equal to zero if the bond is broken (it has surpassed the critical bond stretch, or it was originally broken due to a pre-existing crack) and it mathematically can be shown as [34]:

$$\mu(t, \boldsymbol{\xi}) = \begin{cases} 1 & if\ s(t', \boldsymbol{\xi}) < s_0 \ \forall\ 0 \le t' \le t \\ 0 & otherwise \end{cases} \quad . \tag{10}$$

From this failure criterion, a peridynamic damage parameter is proposed as a value that can range from zero (none of the material point's bonds are broken) to unity (all the bonds of the material points have broken). The equation for damage is then defined as unity minus the ratio of healthy bonds to the original number of nodes in the neighborhood, or:

$$\varphi(\boldsymbol{x},t) = 1 - \frac{\int_{H_x} \mu(\boldsymbol{x},t,\boldsymbol{\xi}) dV_{\boldsymbol{\xi}}}{\int_{H_x} dV_{\boldsymbol{\xi}}} \quad . \tag{11}$$

In continuation of the constitutive model, Silling [34] obtained the expression for the micromodulus, *c,* by equating the continuum-mechanics strain energy density expression for a linear-elastic material under isotropic expansion (W_{CM}):

$$W_{CM} = \frac{9ks^2}{2} \quad , \tag{12}$$

to that of the peridynamic model (W_{PD}):

$$W_{PD} = \frac{1}{2}\int_{H_x} w(\boldsymbol{\eta},\boldsymbol{\xi}) dV_{\xi} = \frac{1}{2}\int_0^{\delta} \left(\frac{cs^2\xi}{2}\right) 4\pi\xi^2 d\xi = \frac{\pi c s^2 \delta^4}{4} \quad , \tag{13}$$

where *k* is the bulk modulus. Thus, for a three-dimensional case, by equating Eq. (12) to Eq. (13), the micromodulus expression is found as:

$$c = \frac{18k}{\pi\delta^4} \quad . \tag{14}$$

It's important to note that given the pairwise nature of the bond forces acting only along the current bond direction, the Poisson's ratio is "locked" with a value of 1/4 for 3D and plane strain conditions, and to a value of 1/3 for plane stress conditions. The expression for the micromodulus in each case is as follows [47]:

$$c = \begin{cases} \dfrac{6E}{\pi h\delta^4(1-2\nu)} & \left(\nu = \dfrac{1}{4}\right) \quad 3D \\ \dfrac{6E}{\pi h\delta^3(1-\nu)} & \left(\nu = \dfrac{1}{3}\right) \quad plane\ stress \\ \dfrac{6E}{\pi h\delta^3(1+\nu)(1-2\nu)} & \left(\nu = \dfrac{1}{4}\right) \quad plane\ strain \end{cases} \quad , \tag{15}$$

where *E* is the Young's modulus, ν is the Poison's ratio, and *h* is the specimen thickness. A similar procedure is needed to find the critical bond stretch, s_0. In this case, Silling's approach was to

equate the energy required to open a unit area of a crack surface, to the peridynamic energy needed to break all the bonds joining two points across this surface (Fig. 2). In 3D, the fracture toughness of a material can be related to the critical bond stretch through the following expression [17, 20]:

$$G_o = \int_0^{\delta}\int_0^{2\pi}\int_z^{\delta}\int_0^{\cos^{-1} z/\xi} \left(\frac{cs_0^2\xi}{2}\right)\xi^2 sin\phi d\phi d\phi d\xi d\theta dz \quad , \tag{16}$$

leading to:

$$s_0 = \sqrt{\frac{5G_0}{9k\delta}} = \sqrt{\frac{5G_0(1-2\nu)}{3E\delta}} = \sqrt{\frac{5G_0}{6E\delta}} \qquad with \;\; \nu = \frac{1}{4} \;\; . \tag{17}$$

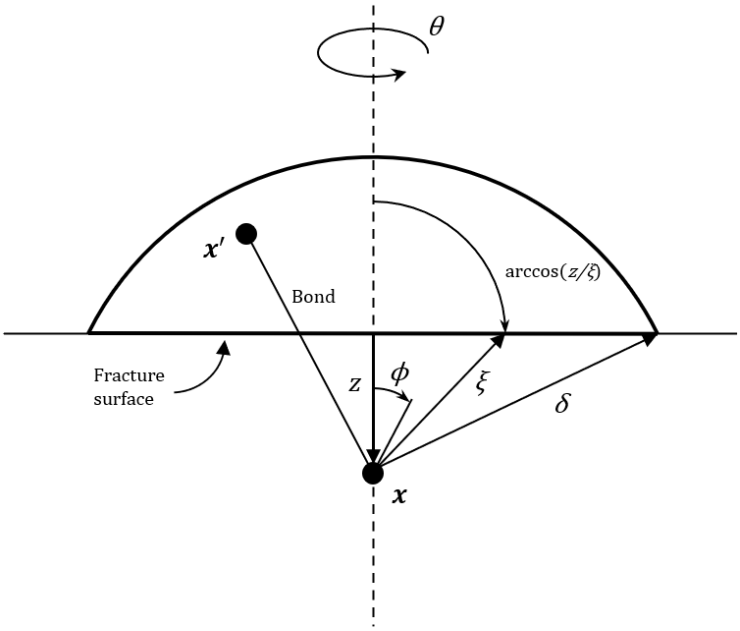

Fig. 2. Physical representation for the computation of critical peridynamic bond stretch based on fracture energy.

Similarly, for the plane stress conditions, the expression for the critical bond stretch is [70, 71]:

$$s_0 = \sqrt{\frac{4\pi G_0}{9E\delta}} \quad plane\ stress\ \left(\nu = \frac{1}{3}\right) \;\; . \tag{18}$$

However, this approach has three major limitations; a fixed value for Poisson's ratio that is problem-dependent, the inability of the bonds to experience anything except axial loads, and the failure criterion being based only on axial extension/compression of these bonds. All three of these lead to an inaccurate representation of dynamic crack initiation, propagation, and bifurcation,

especially in materials with a different Poisson's ratio and mixed-mode loading where shear effects are predominant. The rest of this paper focuses on modifying the original bond-based peridynamics by treating the bonds as Timoshenko beams instead of linear springs to overcome the existing issues.

2.2. Proposed 2D Timoshenko-Based Peridynamics

Due to the previously stated issues of BBPD, and the computational cost of the more advanced SBPD models, extensive research has been undertaken to improve the original BBPD model in order to add more degrees of freedom to the bonds, such as the work carried out by Gerstle's MPPD [40, 60, 61], which treated the bonds as Euler-Bernoulli beams. Gerstle's approach partly solves the Poisson's ratio issue of BBPD, being limited to Poison's ratios up to 1/4 only, and adds a rotational degree of freedom to the particles, leading to a more accurate representation of the linear elastic material's behavior. Nevertheless, the Euler-Bernoulli beam theory is mostly suitable for high aspect ratio beams and neglects shear deformation, making it insensitive to the deviatoric part of deformation, failing to capture shear-dominated fracture scenarios (Fig. 3). Thus, further efforts have been made to improve the peridynamic model by using modified versions of Timoshenko beam theory adapted for this numerical method which led to the addition of shear stiffness and rotational stiffness coefficient [47, 61]. However, the purpose of this paper is to use the exact Timoshenko stiffness matrix with a peridynamic equivalent of the shear influence factor and reduce the number of stiffness coefficients to tensile and shear (similarly to Gerstle's [60, 61] work and to classical continuum mechanics where material properties are characterized through the Young's and shear moduli). Given that the particles are now not only allowed to have linear displacement but can also rotate, the new peridynamic equations of motion are:

$$\rho\ddot{\boldsymbol{u}}(\boldsymbol{x},t) = \int_{H_x} \boldsymbol{f}\left(\boldsymbol{\eta},\boldsymbol{\xi},\theta_i,\theta_j\right)dV_{\boldsymbol{x}'} + \boldsymbol{b}(\boldsymbol{x},t) \quad , \tag{19}$$

$$J_\rho\ddot{\boldsymbol{\theta}}(\boldsymbol{x},t) = \int_{H_x} \boldsymbol{m}\left(\boldsymbol{\eta},\boldsymbol{\xi},\theta_i,\theta_j\right)dV_{\boldsymbol{x}'} + \boldsymbol{n}(\boldsymbol{x},t) \quad , \tag{20}$$

where $\ddot{\theta}$ is the angular acceleration of the particle, $\boldsymbol{n}$ is an external body moment density field, $\boldsymbol{m}$ is a pairwise moment vector in units of force times length per unit volume squared, and J_ρ is the specific angular mass moment of inertia of a particle.

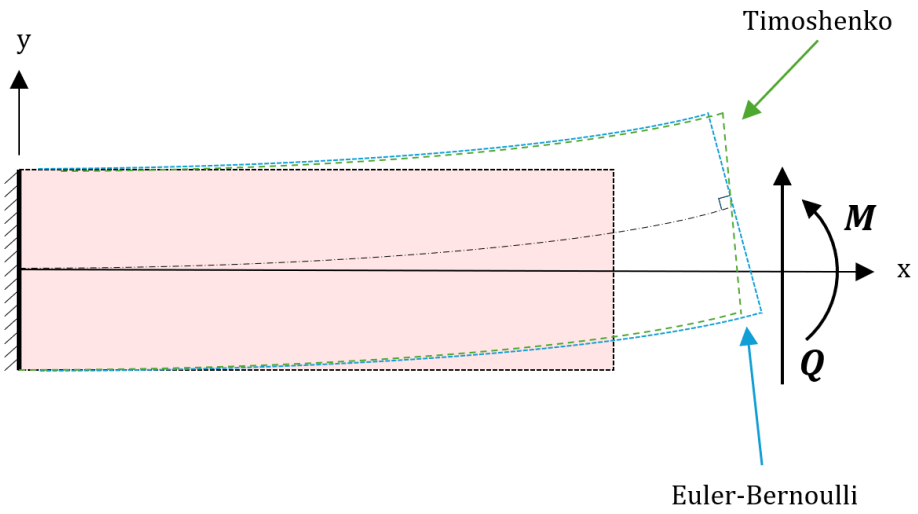

Fig. 3. Euler-Bernoulli and Timoshenko beam deformation comparison under shear loads.

For a two-node, 2D beam, there are two pairwise translational and one pairwise rotational degree of freedom, thus, the Timoshenko stiffness matrix reduces to a six-by-six matrix:

$$\begin{Bmatrix} f_{xi} \\ f_{yi} \\ m_{zi} \\ f_{xj} \\ f_{yj} \\ m_{zj} \end{Bmatrix} = \begin{bmatrix} \frac{EA}{L} & 0 & 0 & -\frac{EA}{L} & 0 & 0 \\ 0 & \frac{12EI_x}{(1+\varphi_x)L^3} & \frac{6EI_x}{(1+\varphi_x)L^2} & 0 & -\frac{12EI_x}{(1+\varphi_x)L^3} & \frac{6EI_x}{(1+\varphi_x)L^2} \\ 0 & \frac{6EI_x}{(1+\varphi_x)L^2} & \frac{(4+\varphi_x)EI_x}{(1+\varphi_x)L} & 0 & -\frac{6EI_x}{(1+\varphi_x)L^2} & \frac{(2-\varphi_x)EI_x}{(1+\varphi_x)L} \\ -\frac{EA}{L} & 0 & 0 & \frac{EA}{L} & 0 & 0 \\ 0 & -\frac{12EI_x}{(1+\varphi_x)L^3} & -\frac{6EI_x}{(1+\varphi_x)L^2} & 0 & \frac{12EI_x}{(1+\varphi_x)L^3} & -\frac{6EI_x}{(1+\varphi_x)L^2} \\ 0 & \frac{6EI_x}{(1+\varphi_x)L^2} & \frac{(2-\varphi_x)EI_x}{(1+\varphi_x)L} & 0 & -\frac{6EI_x}{(1+\varphi_x)L^2} & \frac{(4+\varphi_x)EI_x}{(1+\varphi_x)L} \end{bmatrix} \begin{Bmatrix} u_i \\ v_i \\ \theta_i \\ u_j \\ v_j \\ \theta_j \end{Bmatrix}, \quad (21)$$

where f_x, f_y, and m_z are the axial force, transversal force, and out-of-plane moment, respectively. The subfix i and j denote the node at the coordinate system and at the end of the beam (cf., Fig. 3), respectively (or in the peridynamic sense, the node of interest and its neighbor). The geometrical parameters L, A, and I_x refer to the length, cross-sectional area, and second moment of inertia of the beam respectively. Furthermore, to predict the shear deformation, the shear influence factor, φ_x, is defined as follows:

$$\varphi_x = \frac{12EI_x}{k_s AGL^2} \quad , \tag{22}$$

where G is the shear modulus and k_s is the shape factor for the cross-sectional area of the beam. For the purposes of this study, the "cross-section" of the bond is assumed to be circular, thus, the shape factor has a value of 10/9 [61].

It is worth noting that in the peridynamic framework, material properties such as Young's modulus and shear modulus do not appear explicitly, and the bonds do not have a known cross-sectional area or a second moment of inertia. Instead, the tensile and shear stiffness coefficients encompass these characteristics and are, from now on, defined as $c = EA$, and $\kappa = EI_x$, respectively. Furthermore, the length of the bond in the undeformed configuration, ξ, corresponds to the beam length. Given that the sum of all forces and moments from all bonds attached only to the node of interest is needed to compute its acceleration, the Timoshenko stiffness matrix can be truncated to a six-by-three matrix as such:

$$\begin{Bmatrix} f_{xi} \\ f_{yi} \\ m_{zi} \end{Bmatrix} = \begin{bmatrix} \frac{c}{\xi} & 0 & 0 & -\frac{c}{\xi} & 0 & 0 \\ 0 & \frac{12\kappa}{(1+\varphi_x)\xi^3} & \frac{6\kappa}{(1+\varphi_x)\xi^2} & 0 & -\frac{12\kappa}{(1+\varphi_x)\xi^3} & \frac{6\kappa}{(1+\varphi_x)\xi^2} \\ 0 & \frac{6\kappa}{(1+\varphi_x)\xi^2} & \frac{(4+\varphi_x)\kappa}{(1+\varphi_x)\xi} & 0 & -\frac{6\kappa}{(1+\varphi_x)\xi^2} & \frac{(2-\varphi_x)\kappa}{(1+\varphi_x)\xi} \end{bmatrix} \begin{Bmatrix} u_i \\ v_i \\ \theta_i \\ u_j \\ v_j \\ \theta_j \end{Bmatrix} \quad . \tag{23}$$

This novel recasting of the MPPD Timoshenko stiffness matrix maintains the shear influence factor as a length-dependent variable, similar to the original Timoshenko stiffness matrix. Thus, shorter bonds will be subjected to higher and more accurate shear forces, leading to earlier failure as compared to previous MPPD models where this differentiation was not accounted for. Assuming local isotropy, using the relationship between the Young's modulus and shear modulus, the shear influence factor is reformulated in peridynamic form as:

$$\varphi_x = \frac{12EI_x}{k_s AGL^2} = \frac{12EI_x}{\frac{10}{9}AL^2} \times \frac{2(1+\nu)}{E} = \frac{108\kappa(1+\nu)}{5c\xi^2} \quad . \tag{24}$$

Now, the Timoshenko beam theory has been implemented into the peridynamic framework, adding one translational and one rotational degree of freedom for a 2D case (Fig. 4). To obtain the two

stiffness constants in terms of the classical material properties, the strain energy density expression from continuum mechanics is equated to the new expression found from Timoshenko MMPD in terms of the unknown constants. For the case of isotropic expansion (uniform strain field), the bonds are only stretched axially, and no shear effects are seen. Thus, following the same procedure as Silling [34], the same axial micromodulus equation as in Eq. (15) is obtained. To acquire the expression for the shear micromodulus, a similar procedure is followed but applying a uniform shear field. The micropotential is then described by Eq. (25) as:

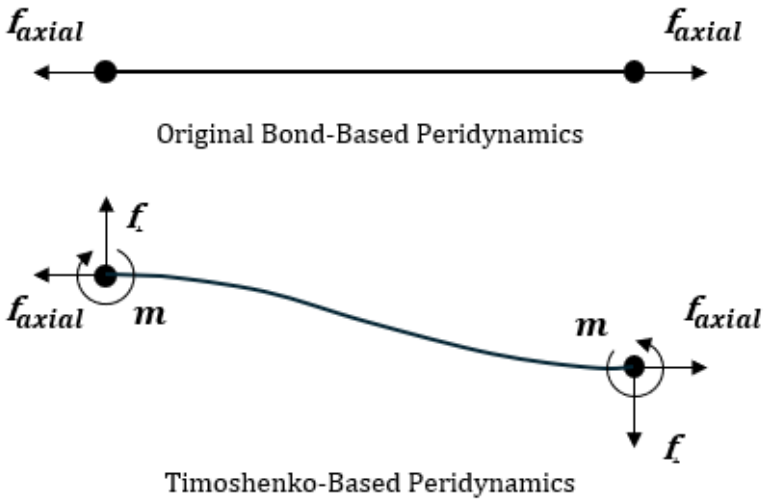

Fig. 4. Degrees of freedom on original bond-based and Timoshenko-based peridynamics.

$$w = \frac{1}{2} d^T \begin{bmatrix} \frac{c}{\xi} & 0 \\ 0 & \frac{12\kappa}{\xi^3(1+\varphi_x)} \end{bmatrix} d \quad , \tag{25}$$

where d is the two-node's beam displacement vector, and the strain energy density is computed using Eq. (7). Originally, in 2D, this is a one-by-six vector holding the two translational and one rotational degrees of freedom of both nodes, but under the assumption of isotropic expansion around the node of interest, this can effectively be reduced to a one by two vector [65]. Thus,

$$d = [u_i \quad v_i \quad \theta_i \quad u_j \quad v_j \quad \theta_j] \quad , \tag{26}$$

becomes,

$$d = [u_j \quad v_j] = [\gamma_{xy}\xi sin2\phi \quad \gamma_{xy}\xi cos2\phi] \quad , \tag{27}$$

where γ_{xy} is the shear strain, and ϕ is the counterclockwise angle between the bond and the positive x-axis. Next, the local peridynamic strain energy density is computed as:

$$W_{PD} = \frac{h}{4}\int_0^{\delta}\int_0^{2\pi} d^T \begin{bmatrix} \frac{c}{\xi} & 0 \\ 0 & \frac{12\kappa}{\xi^3(1+\varphi_x)} \end{bmatrix} d\xi \, d\phi d\xi \quad . \tag{28}$$

Integrating, the peridynamic strain energy density becomes,

$$W_{PD} = \frac{h}{4}\left[\frac{c\pi\delta^3}{12} + \frac{12\kappa\pi\delta}{\varphi_x + 1}\right]\gamma_{xy}^2 \quad . \tag{29}$$

For plane stress conditions, the strain energy density from continuum mechanics is:

$$W_{CM} = \frac{1}{2}\{0 \quad 0 \quad \gamma_{xy}\}\frac{E}{1-\nu^2}\begin{bmatrix} 1 & \nu & 0 \\ \nu & 1 & 0 \\ 0 & 0 & \frac{1-\nu}{2} \end{bmatrix}\begin{Bmatrix} 0 \\ 0 \\ \gamma_{xy} \end{Bmatrix} = \frac{E}{1-\nu}{\gamma_{xy}}^2 \quad . \tag{30}$$

Equating the terms in Eqs. (29) and (30), and solving for the shear micromodulus, the expression for plane stress conditions becomes:

$$\kappa = \frac{E(1-3\nu)(\varphi_x+1)}{24\pi h\delta(1-\nu^2)} \quad . \tag{31}$$

The shear stiffness coefficient is derived from an innovative formulation that incorporates sliding deformations in accordance with Timoshenko's beam theory. This is accomplished by accounting for the length-dependent shear influence factor. The model accommodates a broad spectrum of Poisson's ratios, unlike the original BBPD, which resulted in a fixed value for this material property. Nevertheless, similarly to other MPPD models, there is a Poisson's ratio upper limit. Gerstle's MPPD model presented a lower upper limit of 1/4 [60, 61], while previous MPPD models utilizing adaptations of the Timoshenko theory without an explicit formulation of the shear influence factor also show an upper limit of 1/3 for this property [64, 65]. It is worth noting that this range covers a grand majority of isotropic brittle materials, which usually have values between 0.15 to 0.33. Substituting Eqs. (15) and (31) into Eq. (24), the shear influence factor is reformulated as:

$$\varphi_x = \frac{1}{\frac{20}{3(1-3\nu)}\left(\frac{\xi}{\delta}\right)^2 - 1} \quad , \tag{32}$$

which is now only a function of the bond length, the horizon radius, and the Poison's ratio. As seen in Fig. 5, the peridynamic shear influence factor behaves very similarly to Timoshenko's shear influence factor as the length of the beam changes and all other variables are held constant. For comparison purposes, the shear influence factor in both cases was computed using equivalent geometrical properties by matching the axial stiffness coefficient previously defined as $c = EA$.

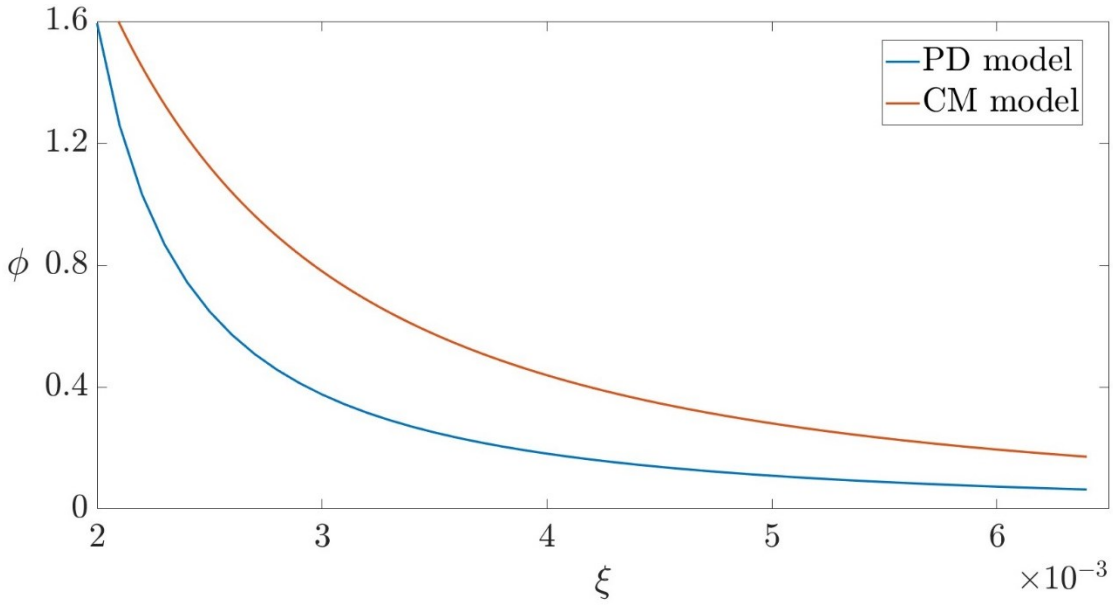

Fig. 5. Classical Timoshenko vs MPPD shear influence factor. Bond length ranges from Δx = 0.002m to 0.0064 m.

Similarly, using the beam analogy once again, the critical shear strain of a bond is related to the critical axial strain as follows:

$$\gamma_0 = \frac{s_0 c \xi^2}{12\kappa} \quad , \tag{33}$$

where γ is defined as,

$$\gamma = \frac{v_j - v_i}{\xi} \quad . \tag{34}$$

Then, the proposed method is implemented by discretizing Eqs. (19) and (20), turning the integral over the horizon into a summation of the contribution of each neighboring node to the forces and moments as follows:

$$\rho \ddot{\boldsymbol{u}}_i^n = \sum_{j=1}^{m} \boldsymbol{f}\left(\boldsymbol{u}_m^n - \boldsymbol{u}_i^n, \boldsymbol{x}_n - \boldsymbol{x}_i, \theta_i, \theta_j\right) V_j + \boldsymbol{b}_i^n \quad , \tag{35}$$

$$J_\rho \ddot{\boldsymbol{\theta}}_i^n = \sum_{j=1}^{m} \boldsymbol{m}\left(\boldsymbol{u}_m^n - \boldsymbol{u}_i^n, \boldsymbol{x}_n - \boldsymbol{x}_i, \theta_i, \theta_j\right) V_j + \boldsymbol{n}_i^n \quad , \tag{36}$$

where n is the time step, and the subscripts denote the node number, so that

$$\boldsymbol{u}_i^n = \boldsymbol{u}(\boldsymbol{x}_i, t^n) \quad . \tag{37}$$

Comparably to the approach used in finite element methods, in peridynamics the stresses are applied as an external force per unit volume acting on the surface nodes, represented by the term $\boldsymbol{b}_i^n$ in Eq. (35). Once the acceleration is computed, the explicit time integration to find the new position and velocity is done using the Velocity-Verlet algorithm [70]:

$$\dot{\boldsymbol{u}}_{n+\frac{1}{2}} = \dot{\boldsymbol{u}}_n + \frac{\Delta t}{2} \ddot{\boldsymbol{u}}_n \ , \tag{38}$$

$$\boldsymbol{u}_{n+\frac{1}{2}} = \boldsymbol{u}_n + \Delta t \dot{\boldsymbol{u}}_{n+\frac{1}{2}} , \tag{39}$$

$$\dot{\boldsymbol{u}}_n = \dot{\boldsymbol{u}}_{n+\frac{1}{2}} + \frac{\Delta t}{2} \ddot{\boldsymbol{u}}_{n+1} \ , \tag{40}$$

where $n + \frac{1}{2}$ denotes a half time step, and Δt is the time step size.

3. Results and Discussion

In this section, the performance of the new Timoshenko MPPD is first compared to a benchmark elastic solution and later to the original BBPD, and the extended non-ordinary SBPD under in-plane dynamic loading conditions. The numerical outcomes are then verified against experimental results for well-known benchmark problems obtained from the literature, such as dynamic branching under pure mode I and the Kalthoff-Winkler experiment for mixed-mode dynamic fracture [72-76]. Later, the effects of varying Poisson's ratio and loading rates on crack paths are investigated using the proposed model.

3.1. Benchmark Elastic Problem

A known isotropic linear-elastic benchmark problem is solved in this section using the proposed Timoshenko-based MPPD model and verified against the FEM analysis. Fig. 6 shows the boundary conditions for the problem.

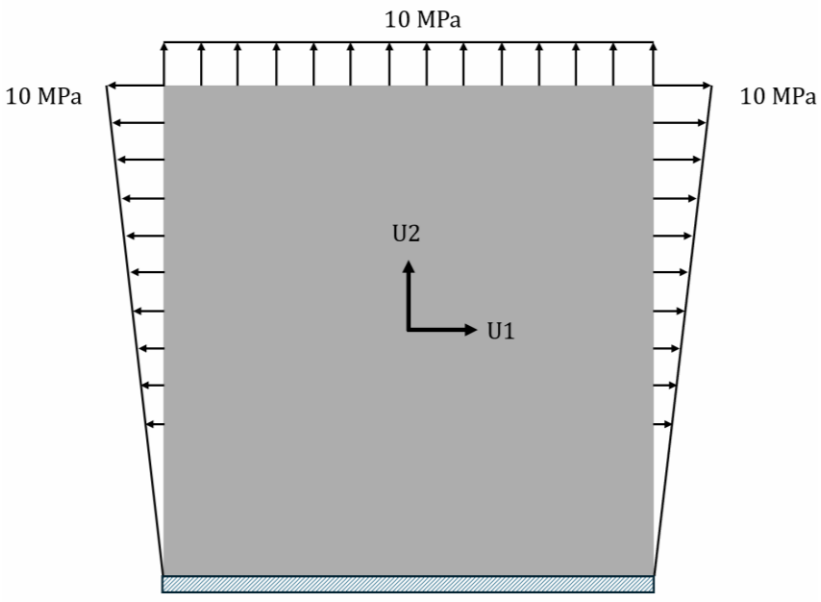

Fig. 6. Elasticity benchmark problem BC's.

Similarly to the work done in [47], the square plate has a Young's modulus of 70 GPa and a Poisson's ratio of 0.25. The structured mesh has a size of $\Delta x = 0.01$ m, and the horizon radius was chosen to be $\delta = 3\Delta x$. Fig. 7 shows the results for both the proposed model and the FEM solution.

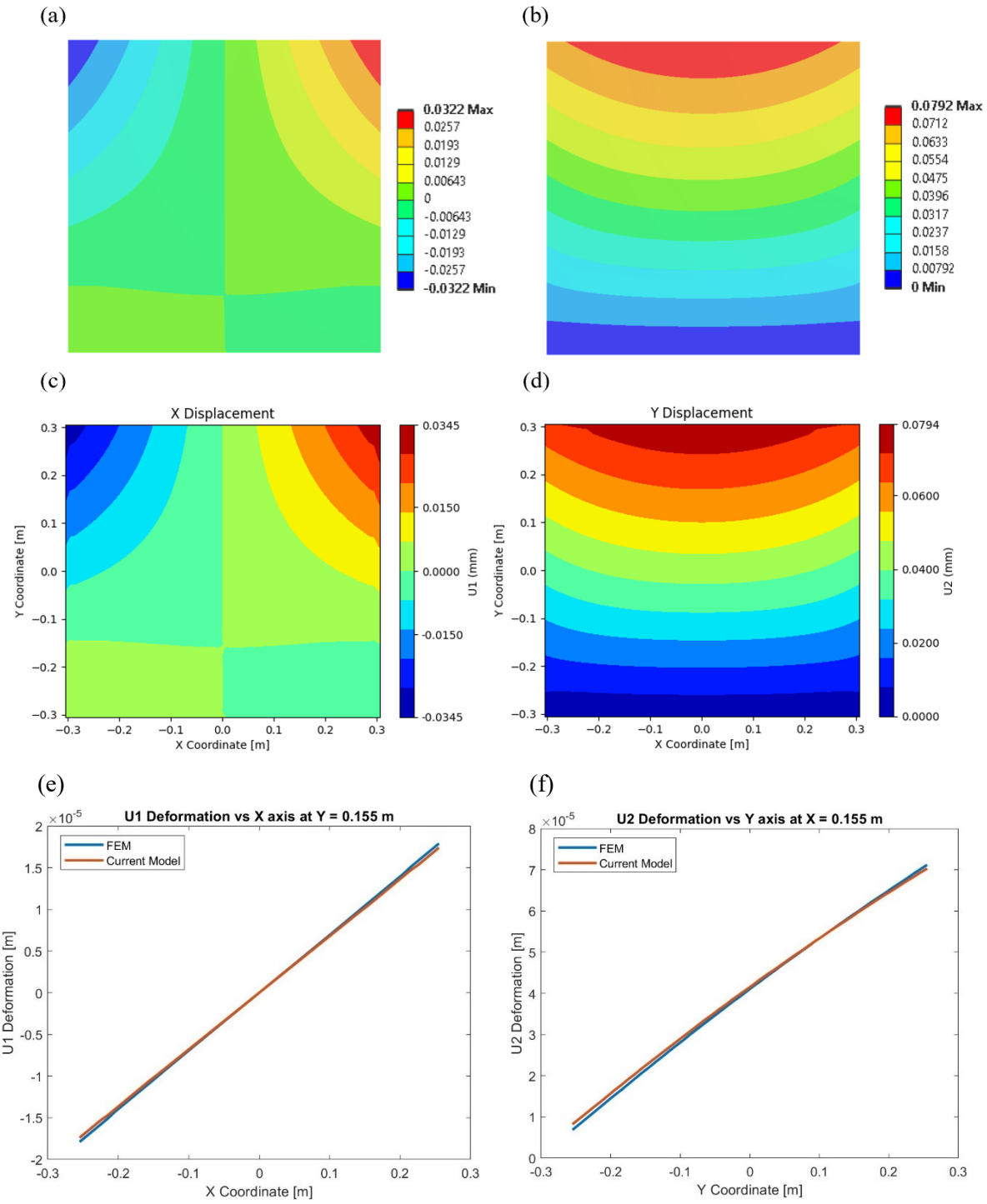

Fig. 7. Elastic benchmark problem solution from FEM for a) x-displacement, b) y-displacement, and the proposed model for c) x-displacement, d) y-displacement in addition to the comparison along y=0.155m for e) x-displacement, and along x=0.155m for f) y-displacement.

It is apparent that the displacement field is accurately approximated by the proposed model. As can be seen in Fig. 7a and 7c, the maximum x-displacement is 0.0322 mm and 0.0345 mm, respectively, denoting a 7.1% error. In the y-direction, Fig. 7b and 7d show a maximum displacement of 0.0792 mm and 0.0794 mm, indicating a 0.25% error. Moreover, the average percent error along the vertical line located at x = 0.155 m, is 3.25% and the average percent error along the horizontal line placed at y = 0.155 m is 2.19%. These lines were chosen with the intention to investigate discrepancies in high gradient regions away from the edges. Regarding maximum percent error, at the vertical line, the y-displacement percent error is 19.9% and in the horizontal line the x-displacement percent error is 2.8%. It is worth noting that the high maximum error in the vertical line is due to small deformation values involved in this location, which is close to the fixed boundary. The displacement discrepancy at this point, however, is only 1.37×10^{-6} m, which is a 0.002% when compared to the maximum displacement. Given that the mesh size and peridynamic horizon are the same as in other MPPD models, it shows that the variable shear influence factor has a significant impact over the results. For instance, in the work done in [47], the maximum error was around 15%. Indeed, while the presented model demonstrates high accuracy in predicting FEM results, its performance may slightly vary depending on the problem size and other discretization parameters.

3.2. Pure Mode I Dynamic Branching

To investigate the validity of the presented model, a benchmark problem illustrated in Fig. 8 is simulated using the proposed Timoshenko MPPD, and compared to results obtained from original BBPD, extended NO-SBPD, and experiments. Table 1 summarizes the material properties of Duran 50, which is used for this model.

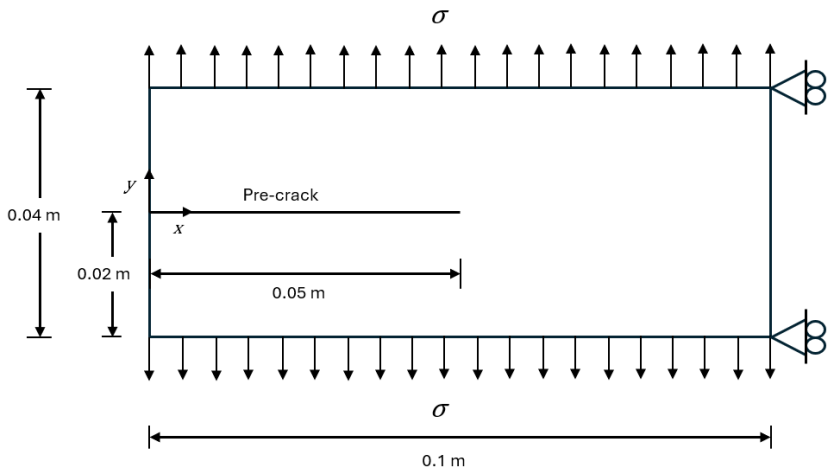

Fig. 8. Loading and boundary conditions for mode I dynamic brittle fracture on edge-crack specimen.

Table 1. Duran 50 material properties [77].

Young's Modulus, *E* (GPa)	Poisson's Ratio	Density (kg/m^3)	Fracture Energy, G_0 (kJ/m^2)
65	0.2	2235	0.2

The test sample consists of a thin 10 by 4 cm plate with a 5 cm edge crack. Duran 50 is a brittle material commonly used in this benchmark problem, both in numerical and experimental tests [70, 71, 72, 76], and thus it is chosen for the validation of the proposed model herein. The sample is symmetrically loaded with a sudden stress of 12 MPa on the upper and lower edges while preventing displacement on the *x*-direction of the rightmost edge. As described in [71] and [77], peridynamic models are sensitive to the choice of grid size and horizon radius. A highly refined mesh with a large horizon radius would lead to extremely long computational time while not necessarily obtaining a significantly better solution than a simpler model with a lesser number of nodes and a shorter horizon radius. Thus, two types of convergence analysis are performed to find an optimal grid size and horizon radius, the m-convergence and the δ-convergence. For the m-convergence, the horizon radius δ is kept constant while the grid size is changed, while for the δ-convergence, the ratio between the horizon radius and the grid size is kept constant, and the grid size is changed. Fig. 9 shows both convergence analyses, with the δ-convergence on the top (Fig. 9a and 9b), and the m-convergence on the bottom (Fig. 9c and 9d).

The δ-convergence analysis was performed by fixing the horizon-to-grid size ratio to 4 (i.e., m = 4) and using two grid sizes (Δx = 0.5 mm and Δx = 0.25 mm), shown in Fig. 9a and 9b,

respectively. Both results show similar crack paths and branching phenomena as expected. However, the computational times are significantly different, with a 20-minute run for the Δx = 0.5 mm grid and 3.5 hours for the Δx = 0.25 mm grid. In the m-convergence analysis, a constant radius of 1.5 mm is chosen, and two grid sizes of Δx = 0.5 mm (m = 3) and Δx = 0.25 mm (m = 6) are used (see Fig. 9c and 9d) [71, 77]. While a more refined mesh (i.e., a larger m-ratio) results in a more concise crack, the overall crack path and crack length are almost identical to the coarser grid, which requires a computational time one order of magnitude smaller. Thus, the grid size of 0.5 mm and the m-ratio of 3.2 will be used for the numerical investigations of this study.

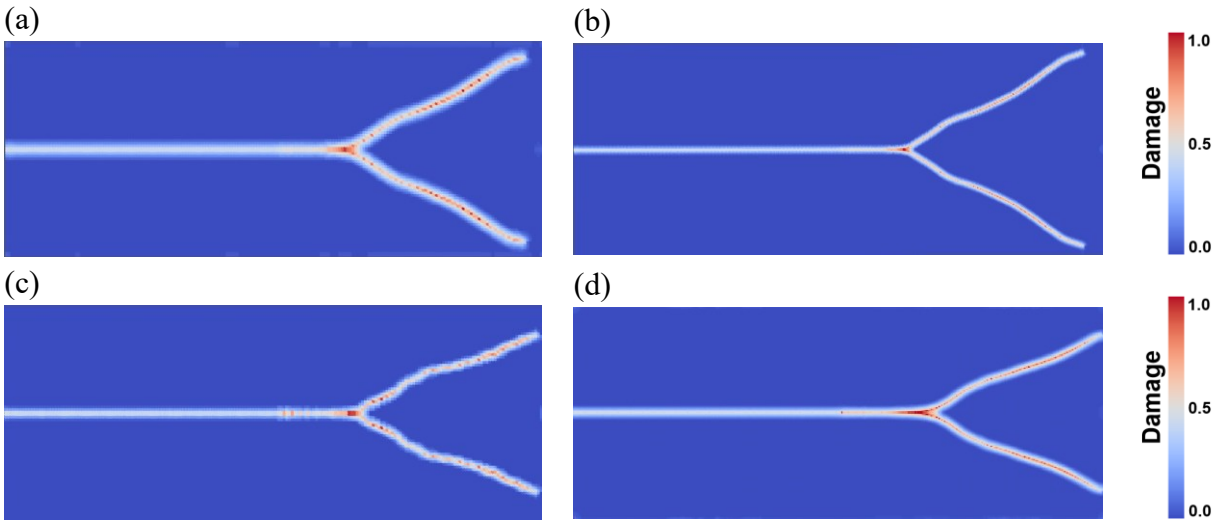

Fig. 9. Study on m-convergence analysis with m = 4 and a) Δx = 0.5 mm, and b) Δx = 0.25 mm. δ-convergence analysis with δ = 1.5 mm and c) Δx = 0.5 mm, and d) Δx = 0.25 mm.

However, to facilitate a better comparison with other numerical methods reported in the literature (see [77]), the grid size for the next model is specifically chosen as Δx = 0.25 mm. This selection aligns with the grid size used in [77], which also has a value of 0.25 mm, resulting in a total of 64,000 discrete material points.

To ensure the numerical stability of the explicit simulation, the time step also needs to be chosen carefully. The maximum time step size is dictated by the time a stress wave requires to propagate through a single grid size unit [34]. In this study, a safety factor of 1/5 is applied as a rule of thumb to guarantee numerical stability and accuracy. Following the work done in [71, 72], the total real simulation time is set to 50 μs, and the horizon radius (δ) is $m \times \Delta x$ where m is equal to 3.2. Note that the m is chosen to be 3.2 as it has been reported in the literature that the values between 3 and 4 yield accurate results with the lowest computational cost [51, 56, 71]. The CPU simulation time

for this model was 3.5 hours on an 11th Gen Intel(R) Core (TM) i7-11850H @ 2.50GHz. Fig. 10 shows the results for all the aforementioned cases at 46 μs, right before the crack propagates through the rightmost edge.

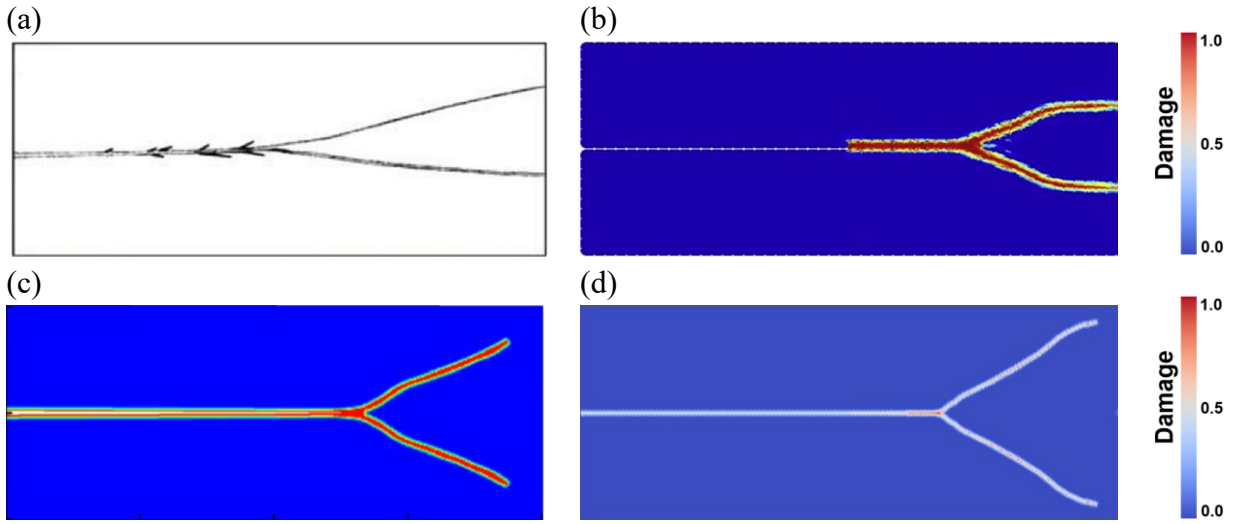

Fig. 10. Pure mode I dynamic crack branching under symmetrical loading (12 MPa) for a) experiment by Ravi-Chandar and Knauss [76], b) extended NOSB [77], c) BBPD [71], and d) the present numerical method.

It is apparent that the present model shows crack propagation and branching as expected from experimental observations and as predicted by both BBPD and extended NO-SBPD models. The initial bifurcation angle is consistent between models as shear effects are not significant on the onset of bifurcation. However, shortly after branching the two new crack tips are subjected to shear forces leading to a gradual change of the crack paths and returning to a horizontal propagation (as observed in Ravi-Chandar's and Knauss' experiment [76]). This phenomenon cannot be seen in the original BBPD results, but it is captured by both the extended NO-SBPD model and the present model.

Fig. 11 shows the crack propagation speed over time for the proposed model, the original BBPD [70], the extended NO-SBPD [77], and the maximum experimental speed [78], using a grid spacing of $\Delta x = 0.5$ mm in all models for a more rigorous comparison between results. As can be seen in this figure, the proposed Timoshenko MMPD model has an overall better performance compared to the other two models considering both the accuracy of the results and the computational time. The maximum crack propagation speed found by the current model was 1708 m/s, which is 8% higher than the maximum theoretical speed, while the original BBPD model shows a 25.6%

overshoot with a maximum velocity of 1985 m/s. The extended NO-SBPD shows a better agreement with the theoretical values at approximately 5% overshoot. However, the presented model is mathematically simpler and hence less computationally expensive for a comparable result.

Note that the crack speed is calculated using the following equation:

$$V_{tip} = \frac{\|\boldsymbol{x}_n - \boldsymbol{x}_{n-1}\|}{t_n - t_{n-1}} \quad , \tag{35}$$

where V_{tip}, $\boldsymbol{x}_n$, $\boldsymbol{x}_{n-1}$, t_n, and t_{n-1}, are the crack tip velocity, the crack tip position in the current and previous time steps, and the real simulation time in the current and previous time steps, respectively.

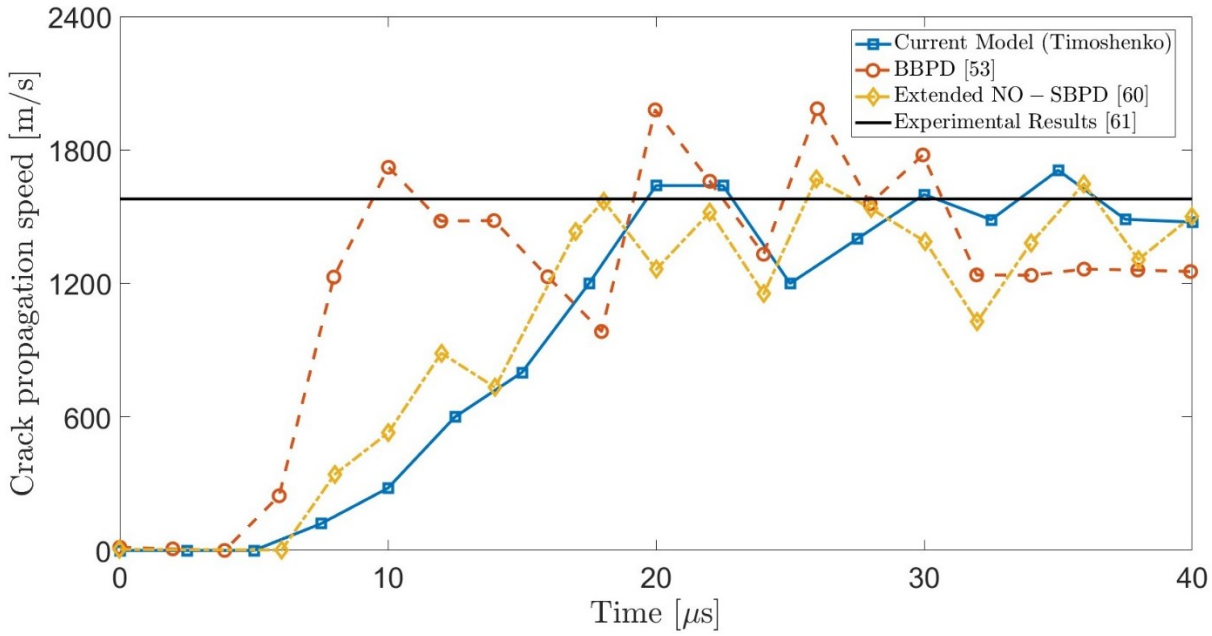

Fig. 11. Crack propagation speed comparison between the proposed model, the original BBPD [70], extended NO-SBPD [77], and the maximum experimental velocity [78].

3.3. Kalthoff-Winkler Experiment

The Kalthoff-Winkler experiment is a well-known benchmark problem for in-plane mixed-mode dynamic crack propagation for which extensive experimental and numerical results can be found in the literature. Fig. 12 illustrates the geometry and boundary conditions for the test setup, which consists of a thin rectangular 100 by 200 mm plate with two symmetrically placed 50 mm edge

cracks, and a velocity constraint is imposed on the edge between the cracks. The material properties are those of maraging steel and can be found in Table 2.

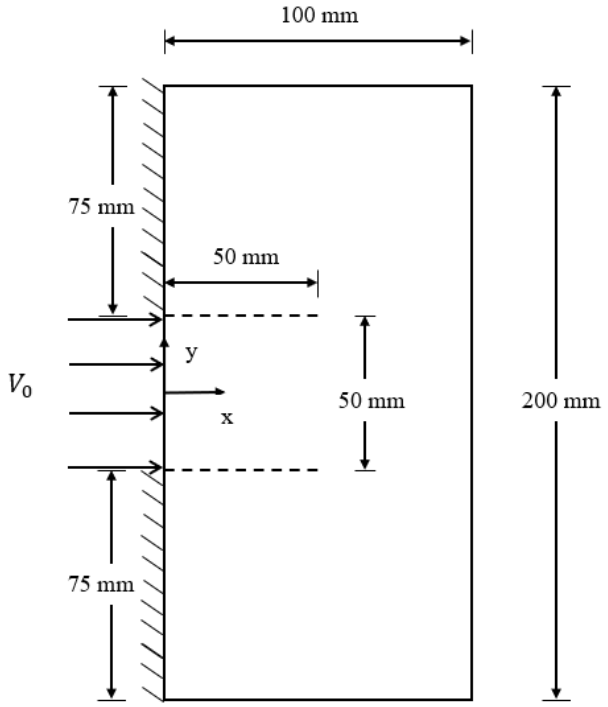

Fig. 12. Boundary conditions for the Kalthoff-Winkler mixed-mode dynamic fracture experiment.

Table 2. Maraging steel material properties [77].

Young's Modulus, *E* (GPa)	Poisson's Ratio	Density (kg/m^3)	Fracture Energy, G_0 (kJ/m^2)
190	0.3	8000	22.17

For a better comparison, in this case, the grid spacing for the numerical simulation is chosen to be the same as in the simulations carried out by Zhou et al. [77], and by Dipasqual et al. [79], where $\Delta x = 1$ mm. The total number of material points is 20,000 and the time step is chosen in the same manner as explained in the previous benchmark example. An initial velocity of 16.5 m/s is applied to the leftmost edge at $-25 \leq y \leq 25$ mm, and the real simulation time is 90 μs. Note that the coordinate system is placed in the middle of the specimen on the left edge. Similarly, the m-ratio between the horizon radius and grid size is set to m = 3.2. Fig. 13 shows the results obtained experimentally, and using XFEM, BBPD, extended NO-SBPD, and the proposed model.

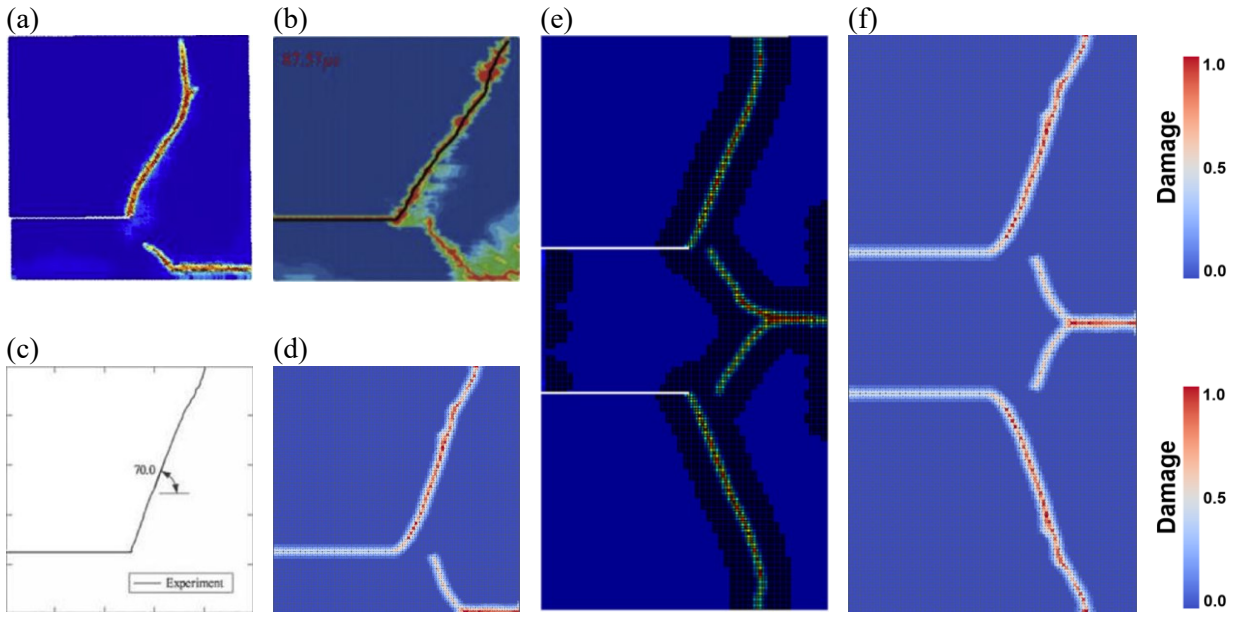

Fig. 13. Results for Kalthoff-Winkler setup a) extended NOSB by Zhou et al. [77], b) XFEM by Belytscho et al. [80], c) original Kalthoff-Winkler experiment [74], d) proposed model, e) BBPD by Dipasqual et al. [79], and f) proposed model for the full specimen.

While the experiment setup is the one described earlier, it is common to apply symmetric boundary conditions at y = 0 and simulate only one-half of the test article to save computational resources as seen in several examples in Fig. 13. For the present study, however, the full test article was simulated as seen in Fig. 13f, and a crop of only the upper part is shown in Fig. 13d for better visualization and comparison.

As expected from classical fracture mechanics and seen in the Kalthoff-Winkler experiment, under in-plane shear-dominant loading conditions, the crack initiation angle is close to 70º [2,5]. All numerical models presented in Fig. 13 capture this phenomenon accurately, with the exception of XFEM having a slightly lower slope. However, there is a noticeable difference towards the end of the simulation as the crack approaches the upper edge. Both BBPD [79] and extended NO-SBPD [77] show the crack path deviating upwards becoming almost vertical towards the edge. However, the original experimental results [74] show the crack maintaining a straight fashion until the end with some minor kinking. This is also seen in the XFEM results [80] but the crack leans towards the end more than the one seen in the experiment or other numerical results. The Timoshenko MPPD model presented here, captures the crack initiation angle, and the entire crack path accurately being almost identical to the experimental results, proving its capabilities to capture shear effects on brittle materials. It is worth noting that while not seen in the experiment carried

out by Kalthoff and Winkler [74], a second crack naturally forms at the center of the specimen on the rightmost edge and starts propagating as a Mode I fracture that later branches symmetrically. This phenomenon is also observed in all other numerical results presented in Fig. 13, exhibiting a similar crack pattern.

3.4 Further Numerical Results

In the following section, the effects of loading rate and Poisson's ratio on mixed-mode dynamic fracture behavior are investigated. The two benchmark problems discussed in Sections 3.2 and 3.3 are subjected to higher stresses and initial velocities respectively while keeping all the rest of the parameters the same for a more insightful qualitative analysis of the effects of higher loading rates. Similarly, the effects of different Poisson's ratios on crack propagation are studied on those same specimens. Finally, the Kalthoff-Winkler experiment setup is modified by changing the crack orientation angles and tested under various initial conditions.

3.4.1 Effects of loading rate

In this section, the effect of loading rate for pure mode I and in-plane loading conditions is investigated by subjecting the specimens from Sections 3.2 and 3.3 to two different loading rates. Additionally, these effects are also investigated in two modified Kalthoff-Winkler setup models.

Under pure mode I conditions, all the material properties and geometrical parameters are identical to the ones mentioned in Section 3.2, except for a coarser grid size of $\Delta x = 0.5$ mm, and a Poisson's ratio of 0.3. The test article was subjected to a sudden load of 20 and 30 MPa as shown in Fig. 14. For the 20 MPa loading case (Fig. 14a), a simple bifurcation pattern with no secondary branching is observed, very similar to previous cases. However, the two crack tips present a sudden change in propagation angle shortly after bifurcation, indicating a more prominent stress wave interference pattern during crack growth. Constructive interference of these waves leads to localized areas with grater stress that the crack tips propagate through. At a higher loading stress of 30 MPa (Fig. 14b), the crack path shows a more complex pattern with secondary branching occurring due to the aforementioned reasons. A higher number of crack fronts at higher loading rates is also expected in order to dissipate the energy in the specimen once the material cannot store any more elastic energy [71].

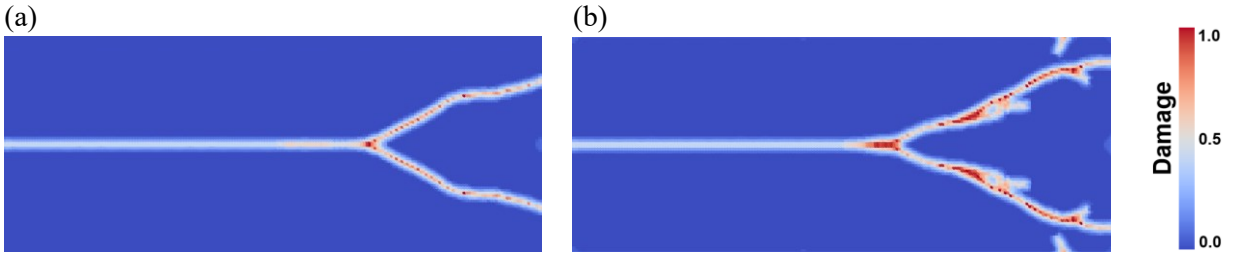

Fig. 14. Dynamic Mode I branching in Duran 50 at a) $\sigma = 20$ MPa and b) $\sigma = 30$ MPa.

For mixed-mode loading conditions, the exact same simulation parameters as in Section 3.3 is used, except for the initial velocities, which is set to 30 and 40 m/s for the analysis (Fig. 15a and 15d, respectively). Two other variations of this test article are modeled for different mode mixities with crack orientation angles of 30º and 60º as shown in Fig. 15b and 15e, and Fig. 15c and 15f, respectively. Both test articles were also subjected to initial velocities of 30 and 40 m/s, as depicted in Fig. 15b and 15c, and Fig. 15e and 15f, respectively.

For the original Kalthoff-Winkler setup configuration, increasing the initial speed to 30 m/s leads to a slightly shallower crack initiation angle [2] and more prominent secondary branching, with secondary cracks forming at nearly right angles from the main branch. This additional branching is not seen in the original experiment at 16.5 m/s. As the crack angle is increased, the crack tip is closer to the edges of the specimen, and the shear deformations are not as significant around the crack tip. It is apparent that branching becomes less prominent as the crack angle is increased and the crack tip starts closer to the upper edge. In the 60º case this phenomenon is not observed and only crack kinking is seen. However, as the crack angle increases, the naturally occurring cracks along the middle of the rightmost edge begin to propagate earlier and branch more extensively, resulting in greater damage and increased energy release in this region. At 40 m/s the crack paths are similar to those seen at 30 m/s, presenting even shallower crack initiation angles and more branching events due to the higher energy dissipation rates required. It is also worth noting that a shear band forms in the configuration displayed in Fig. 15f, where the original crack meets the leftmost edge of the specimen. This shear band formation is similar to the results observed by Diana and Ballarini [46] showing the failure mode switching at higher loading rates.

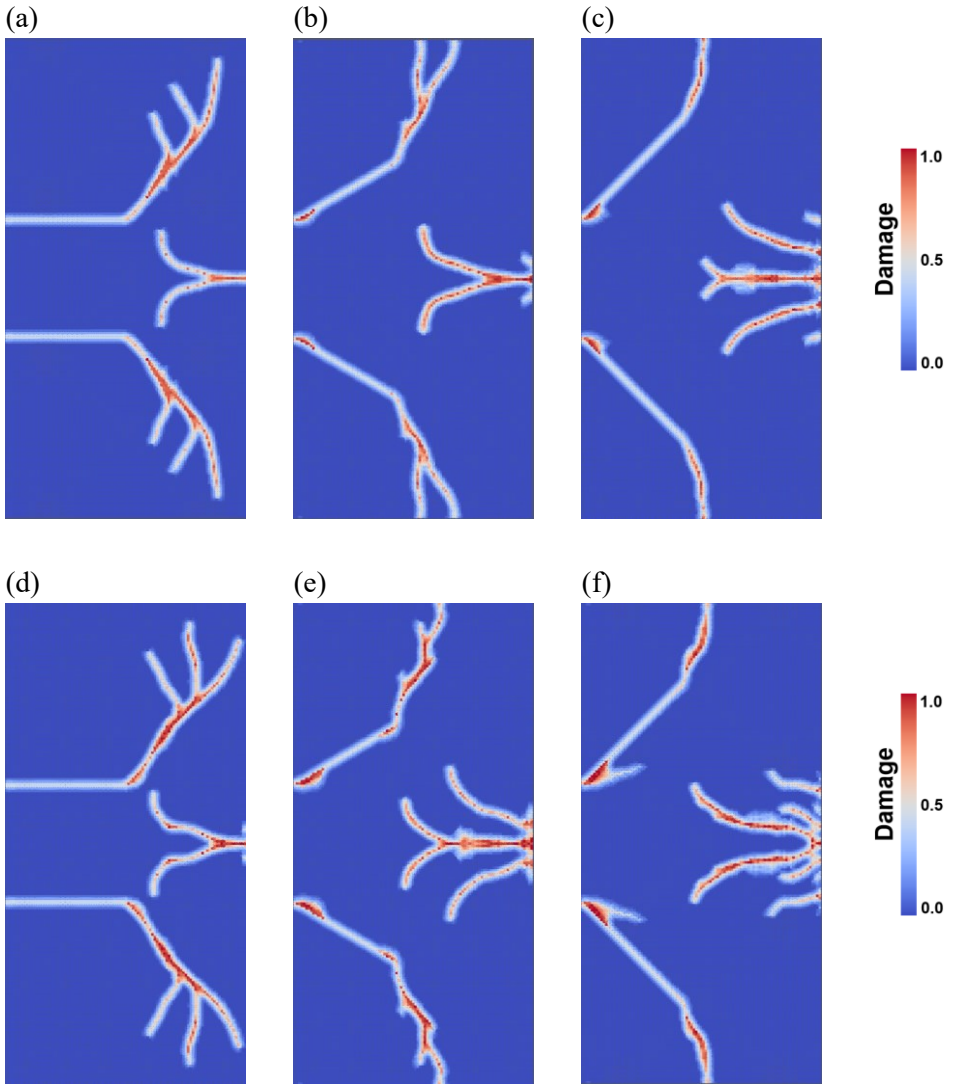

Fig. 15. Dynamic crack propagation in the modified Kalthoff-Winkler setup at 30 m/s for an initial crack angle of a) 0º, b) 30º, c) 60º, and at 40 m/s with an initial crack angle of d) 0º, e) 30º, and f) 60º.

3.4.2. Effects of Poisson's ratio

To investigate the effect of Poisson's ratio on mode I dynamic crack propagation, the simulation setup from Section 3.2 is used ($\sigma = 12$ MPa). The geometrical and boundary conditions are kept the same, the grid size is coarsened to $\Delta x = 0.5$ mm, and the model's prediction is computed for $\nu = 0.1$ and $\nu = 0.25$. The results shown in Fig. 16 indicate a clear dependency between the crack branching initiation and Poisson's ratio, as well as the crack path after bifurcation. The path maintains a consistent propagation angle after bifurcation for lower values of Poisson's ratio, while for higher values the crack presents a tendency to kink towards a horizontal orientation as observed in the results shown in Fig. 14 and Section 3.2. The earlier bifurcation and straight crack paths in

materials with lower Poisson's ratio, arise from its diminishing ability to deform perpendicular to the load direction. Under such circumstances, lesser amounts of work are stored in the form of elastic energy, thus resulting in cracks forming to dissipate the remaining energy. Equally, shear stresses are less prominent during axial loading, resulting in reduced kinking of the crack after branching.

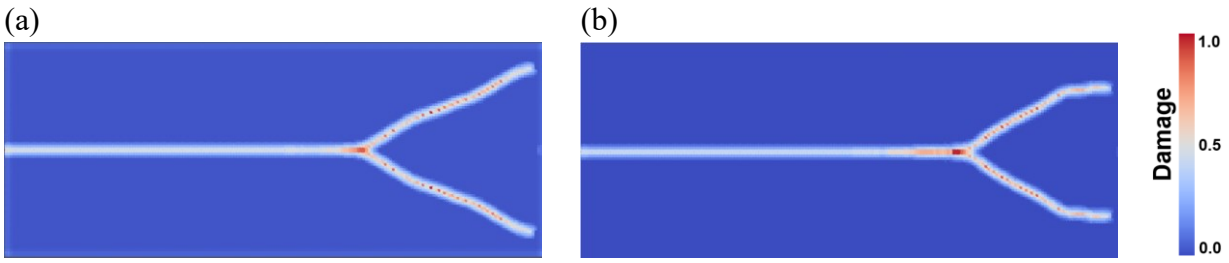

Fig. 16. Dynamic Mode I branching comparison for $\sigma = 12$ MPa a) ν = 0.1 and b) ν = 0.25

For the Kalthoff-Winkler experiment, all geometrical, material, and simulation parameters from Section 3.3 were used with the exception of Poisson's ratio which was tested at values of 0.1 and 0.2. Fig. 15 shows the upper half of the results for both cases. In the case of ν = 0.1, while the crack initiation angle and initial stages of crack propagation are very similar to those seen in Section 3.3 with ν = 0.3, there is a clear difference towards the end of the simulation where the crack branches for the case of ν = 0.1 (which is not seen for higher values). It is also worth noting that naturally occurring secondary crack on the rightmost edge is no longer a single crack that branches out, but it consists of two cracks instead, one that propagates straight right in the middle of the specimen and a second crack that forms right above and curves upwards. When ν = 0.2, the crack path is almost identical to the ν = 0.3 case, showing very small changes in the main crack where initiation of bifurcation can be seen in a similar region observed for ν = 0.1. The secondary crack originating on the rightmost edge presents a similar path to that observed for ν = 0.3, however, crack branching occurs closer to the origin of the crack.

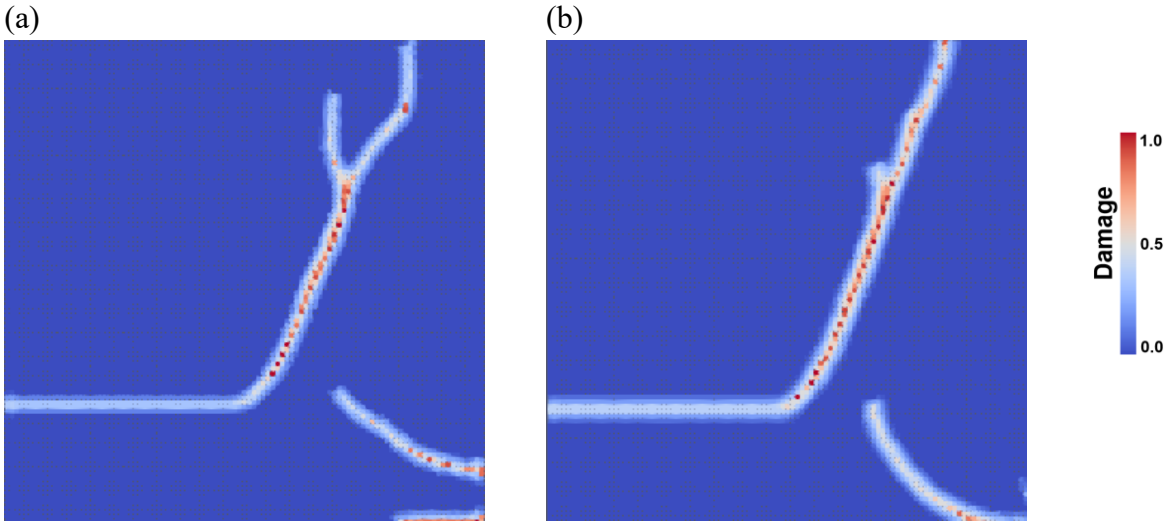

Fig. 17. Dynamic mixed-mode crack propagation comparison for Kalthoff-Winkler experiment at V_0= 16.5 m/s with different Poisson's ratios a) ν = 0.1 and b) ν = 0.2.

4. Conclusion

In this work, a new formulation for Bond-Based Peridynamics (BBPD) is presented by treating the bonds as Timoshenko beams, explicitly considering shear deformation effects, which is particularly important for short beams. This approach is advantageous because it accounts for the effect of shear in the deformation of the bonds, and the subsequent shear failure by incorporating a strain-based criterion which were originally neglected in the traditional BBPD. While previous researchers used the Timoshenko approach to MPPD, the shear influence factor was treated as constant and clustered as part of the shear stiffness coefficient. However, the core novelty of the current study is to consider a length-dependent shear influence factor which better resembles the underlying physics. It was revealed that the suggested Timoshenko Multipolar Peridynamics (MPPD) formulation is in good agreement with the experimental and numerical benchmark problems reported in the literature, denoting the validity and accuracy of the method. The study showed that adding extra degrees of freedom to the problem mitigates the Poisson's ratio limitation in the original BBPD allowing the model to use materials with Poisson's ratios up to 1/3. While not completely resolving this issue, the proposed model addresses a wider range of brittle materials.

The current study comprehensively examined how the loading rate and Poisson's ratio influence dynamic crack propagation and branching. It was observed that the higher loading rates lead to more severe secondary branching due to the higher energy release rates, as well as a change in

crack initiation angle and propagation path. Moreover, this phenomenon can also be explained due to the strong influence of constructive interference of stress waves in the crack front. Furthermore, this study revealed that models with lower Poisson's ratio show more prominent branching events than those with higher values due to the different deformation gradients in the material domain. This phenomenon resulted from the material's limited capacity to deform perpendicular to the principal stretch direction which localizes the strain and induces additional branching. This branching effectively dissipated the energy that the material could no longer absorb elastically. However, this influence is not as severe as that of the loading rate in the formation of secondary branches and crack paths.

Understanding the behavior of brittle materials such as ceramics, glass, rocks, etc., under impact scenarios is crucial during the design phases of structures involved in various industries spanning from civil to aerospace engineering. The simplicity of the proposed model compared to State-Based Peridynamic (SBPD), and higher accuracy than the original BBPD formulation, facilitates its use for research and commercial applications. This work aims to improve predictions at a lower computational cost. Further work should be done to obtain an energy-based shear failure criterion, and to account for orthotropy in the material, expanding the use of the method to more complex materials extensively used in engineering applications.

Acknowledgements

The authors would like to acknowledge National Science Foundation of the United States (NSF), CMMI program, Mechanics of Materials and Structures (award # 2317406) for the financial support of this research

References

[1] Liu W, Hu C, Li L, Zhang X, Peng L, Qiao Y, Yue Z. Experimental study on dynamic notch fracture toughness of V-notched rock specimens under impact loads. Eng Fract Mech 2020;259:108109.

[2] Aliha M, Samareh-Mousavi S, Mirsayar M. Loading rate effect on mixed mode I/II brittle fracture behavior of PMMA using inclined cracked SBB specimen. Int J Solid Struct 2021;232:111177.

[3] Zhou YX, Xia KW, Li XB, Li HB, Ma GW, Zhao J, Zhou ZL, Dai F. Suggested methods for determining the dynamic strength parameters and mode-I fracture toughness of rock materials. Int J Rock Mech Min Sci 2012;49:105–12.

[4] Wada H, Seika M, Kennedy TC, Calder CA, Murase K. Investigation of loading rate and plate thickness effects on dynamic fracture toughness of PMMA. Eng Fract Mech 1996;54(6):805–811.

[5] Sundaram BM, Tippur HV. Dynamic mixed-mode fracture behaviors of PMMA and polycarbonate. Eng Fract Mech 2017;176:186–212.

[6] Yoffe EH. The moving Griffith crack. Philos Mag 1951;42:739–50.

[7] Ball A. On the bifurcation of cone cracks in glass plates. Philos Mag A 1996;73:1093–103.

[8] Dai Y, Liu Y, Qin F, Chao YJ, Berto F. Estimation of stress field for sharp V-notch in power-law creeping solids: An asymptotic viewpoint. Int J Solids Struct 2019;180-181:189–204.

[9] Qiu P, Yue Z, Yang R. Mode I stress intensity factors measurements in PMMA by caustics method: a comparison between low and high loading rate conditions. Polym Test 2019;76:273–285.

[10] Mirsayar MM. On the effective critical distances in three-dimensional brittle fracture via a strain-based framework. Eng Fract Mech 2021;248:107740.

[11] Mirsayar MM, Shahbazian B. An energy-based criterion for mixed-mode I/II/III fracture considering effective critical distances. Eng Fract Mech 2022;272:108674.

[12] Mirsayar M, Shahbazian B. A novel three-dimensional notch fracture criterion via effective critical distances. Int J Mech Sci 2024;109149.

[13] Song JH, Wang H, Belytschko T. A comparative study on finite element methods for dynamic fracture. Comput Mech 2008;42:239–250.

[14] Wu H, Ma G, Xia Y. Experimental study of tensile properties of PMMA at intermediate strain rate. Mater Lett 2004;58(29):3681–3685.

[15] Mirsayar MM, Razmi A, Aliha MRM, Berto F. EMTSN criterion for evaluating mixed mode I/II crack propagation in rock materials. Eng Fract Mech 2018;190:186–197.

[16] Ayatollahi MR, Aliha MRM. Mixed mode fracture in soda lime glass analyzed by using the generalized MTS criterion. Int J Solids Struct 2009;46(2):311–321.

[17] Abraham FF, Brodbeck D, Rudge WE, Xu X. Instability of fracture – a computer-simulation investigation. Phys Rev Lett 1994;73:272–5.

[18] Abraham FF, Brodbeck D, Rudge WE, Xu X. A molecular-dynamics investigation of rapid fracture mechanics. J Mech Phys Solids 1997;45:1595–619.

[19] Marder M, Gross S. Origin of crack-tip instabilities. J Mech Phys Solids 1995;43:1–48.

[20] Belytschko T, Chen H, Xu J, Zi G. Dynamic crack propagation based on loss of hyperbolicity and a new discontinuous enrichment. Int J Numer Methods Engng 2003;58:1873–905.

[21] Xu XP, Needleman A. Numerical simulations of fast crack growth in brittle solids. J Mech Phys Solids 1994;42:1397–434.

[22] Camacho GT, Ortiz M. Computational modeling of impact damage in brittle materials. Int J Solids Struct 1996;33:2899–938.

[23] Ortiz M, Pandolfi A. Finite-deformation irreversible cohesive elements for three-dimensional crack-propagation analysis. Int J Numer Methods Engng 1999;44:1267–82.

[24] Rabczuk T, Belytschko T. Cracking particles: a simplified meshfree method for arbitrary evolving cracks. Int J Numer Methods Engng 2004;61:2316–43.

[25] Zhou F, Molinari JF. Dynamic crack propagation with cohesive elements: a methodology to address mesh dependency. Int J Numer Methods Engng 2004;59:1–24.

[26] Song J, Areias PMA, Belyschko T. A method for dynamic crack and shear band propagation with phantom nodes. Int J Numer Methods Engng.

[27] Song JH, Wang H, Belytschko T. A comparative study on finite element methods for dynamic fracture. Comput Mech 2008;42:239-50

[28] Mcauliffe C, Waisman H. A coupled phase field shear band model for ductile brittle transition in notched plate impacts. Comput Methods Appl Mech Eng 2016;305:173–95.

[29] Borden MJ, Verhoosel CV, Scott MA, Hughes TJR, Landis CM. A phase-field description of dynamic brittle fracture. Comput Methods Appl Mech Eng 2012;217:77–95.

[30] Diehl P, Lipton R, Wick T. A comparative review of peridynamics and phase-field models for engineering fracture mechanics. Comput Mech 69, 1259–1293 (2022).

[31] Ramulu M, Kobayashi AS. Mechanics of crack curving and branching – a dynamic fracture analysis. Int J Fract 1985;27:187–201.

[32] Santillán D, Mosquera JC, Cueto-Felgueroso L. Phase-field model for brittle fracture. Validation with experimental results and extension to dam engineering problems. Eng Fract Mech 2017;178:109–25.

[33] Wu J. A unified phase-field theory for the mechanics of damage and quasi-brittle failure. J Mech Phys Solids 2017;103:72–99.

[34] Silling S A, Askari E. A meshfree method based on the peridynamic model of solid mechanics. Comput Struct 2005;83(17-18):1526–1535.

[35] Silling SA. Reformulation of elasticity theory for discontinuities and long-range forces. J Mech Phys Solids 2000;48:175–209.

[36] Silling SA, Zimmermann M, Abeyaratne R. Deformation of a peridynamic bar. J Elast 2003;73:173–90.

[37] Silling SA. Dynamic fracture modeling with a meshfree peridynamic code. Computat Fluid Solid Mech, Elsevier 2003;641–4.

[38] Silling SA, Askari E. Peridynamic modeling of impact damage. PVP Vol 489, ASME 2004;197–205.

[39] Silling SA, Bobaru F. Peridynamic modeling of membranes and fibers. Int J Non-Linear Mech 2005;40:395–409.

[40] Gerstle W, Sau N, Silling S. Peridynamic modeling of concrete structures. Nucl Eng Des 2007;237(12-13):1250–8.

[41] Butt SN, Timothy JJ, Meschke G. Wave dispersion and propagation in state-based peridynamics. Comput Mech 2017;60:725–738.

[42] Bobaru F, Yang M, Alves LF, Silling SA, Askari E, Xu J. Convergence adaptive refinement and scaling in 1D peridynamics. Int J Numer Methods Eng 2009;77(6):852–877.

[43] Cheng Z, Zhang G, Wang Y, Bobaru F. A peridynamic model for dynamic fracture in functionally graded materials. Compos Struct 2015;133:529-546.

[44] Bažant ZP, Luo W, Chau VT, Bessa MA. Wave dispersion and basic concepts of peridynamics compared to classical nonlocal damage models. J Appl Mech 2016;83(11):111004

[45] Silling S A, Epton M, Weckner O, Xu J, Askari E. Peridynamic States and Constitutive Modeling. J Elast 2007;88(2):151-184.

[46] Diana V, Ballarini R. Crack kinking in isotropic and orthotropic micropolar peridynamic solids. Int J Solids Struct 2020;196–197:76–98.

[47] Yu H, Chen X, Sun Y. A generalized bond-based peridynamic model for quasi-brittle materials enriched with bond tension–rotation–shear coupling effects. Comput Methods Appl Mech Eng 2020;372:113405.

[48] Madenci E, Barut A, Phan N. Bond-Based Peridynamics with Stretch and Rotation Kinematics for Opening and Shearing Modes of Fracture. J Peridyn Nonlocal Model 2021.

[49] Ren H, Zhuang X, Rabczuk T. A new peridynamic formulation with shear deformation for elastic solid. J Micromech Mol Phys 2016;1(2):1650009.

[50] Nooru-Mohamed MB, Schlangen E, van Mier JGM. Experimental and numerical study on the behavior of concrete subjected to biaxial tension and shear. Adv Cement Based Mater 1993;1(1):22–37.

[51] Liu W, Yang G, Cai Y. Modeling of failure mode switching and shear band propagation using the correspondence framework of peridynamics. Comput Struct 2018;209:150–162.

[52] Mirsayar M. A generalized model for dynamic mixed-mode fracture via state-based peridynamics. Fatigue Fract Eng Mater Struct 2023;46(1):244–58.

[53] Silling SA, Weckner O, Askari E, Bobaru F. Crack nucleation in a peridynamic solid. Int J Fract 2010;162:219–27.

[54] Foster J, Silling S, Chen W. An energy based failure criterion for use with peridynamic states. Int J Multiscale Comput Eng 2011;9(6):675–687.

[55] Lehoucq R, Silling S. Force flux and the peridynamic stress tensor. J Mech Phys Solids 2008;56(4):1566–1577.

[56] Silling S, Lehoucq R. Convergence of peridynamics to classical elasticity theory. J Elast 2008;93(1):13–37.

[57] Diana V, Casolo S. A bond-based micropolar peridynamic model with shear deformability: elasticity, failure properties and initial yield domains. Int J Solids Struct 2019;160:201–231.

[58] Diana V, Casolo S. A full orthotropic micropolar peridynamic formulation for linearly elastic solids. Int J Mech Sci 2019;160:140–155.

[59] Voigt W. Theoretische studien über die elasticitätsverhältnisse der krystalle. Abh Ges Wiss Göttingen 1887;34:3–51.

[60] Nikravesh S, Gerstle W. Improved state-based peridynamic lattice model including elasticity, plasticity and damage. Comput Model Eng Sci 2018;116(3):323–47.

[61] Gerstle WH, Sau N, Sakhavand N. On Peridynamic Computational Simulation of Concrete Structures. Spec Publ 2009;245–264.

[62] Boley, BA. On the Accuracy of the Bernoulli-Euler Theory for Beams of Variable Section. ASME J Appl Mech 1963; 30(3): 373–378.

[63] Wu K, Zheng G, Chen G. Extending Timoshenko beam theory for large deflections in compliant mechanisms. J Mech Robot 2023;15(6):061012.

[64] Wang Y, Zhou X, Wang Y, Shou Y. A 3-D conjugated bond-pair-based peridynamic formulation for initiation and propagation of cracks in brittle solids. Int J Solids Struct. 2018;134:89-115.

[65] Yan X, Guo L, Li W. Improved Timoshenko beam-based micropolar peridynamic method incorporating particle geometry. Eng Fract Mech 2021;254:107909.

[66] Banerjee JR, Williams FW. Coupled Bending-Torsional Dynamic Stiffness Matrix of an Axially Loaded Timoshenko Beam Element. Int J Solids Struct 1994;31(6):749–62.

[67] Molina-Villegas JC, Ortega JE. Closed-form solution of Timoshenko frames with semi-rigid connections. Structures 2023;48:212–25.

[68] Li J, Shen R, Hua H, Jin X. Coupled bending and torsional vibration of axially loaded thin-walled Timoshenko beams. Int J Mech Sci 2004;46(2):299–320.

[69] Trageser J, Seleson P. Bond-Based Peridynamics: a Tale of Two Poisson's Ratios. J Peridyn Nonlocal Model 2020;2:278–88.

[70] Ha YD, Bobaru F. Studies of dynamic crack propagation and crack branching with peridynamics. Int J Fract 2010;162(1-2):229–44.

[71] Ha YD, Bobaru F. Characteristics of dynamic brittle fracture captured with peridynamics. Eng Fract Mech 2011;78(6):1156–68.

[72] Zhou X, Wang Y, Qian Q. High-speed crack propagation in a peridynamic framework. Eur J Mech A/Solids 2016;60:277–99.

[73] Kalthoff JF. Shadow optical analysis of dynamic shear fracture. Opt Eng 1988;27(10):835-40.

[74] Kalthoff JF, Winkler S. Failure mode transition at high rates of shear loading. Impact Load Dyn Behav Mater 1988;1:185–95.

[75] Guo JS, Gao WC. Study of the Kalthoff–Winkler experiment using an ordinary state-based peridynamic model under low velocity impact. Adv Mech Eng. 2019;11(5):1687814019852561.

[76] Ravi-Chandar K, Knauss WC. An experimental investigation into dynamic fracture: III. On steady-state crack propagation and crack branching. Int J Fract 1984;26(2):141–54.

[77] Zhou X, Wang Y, Qian Q. Numerical simulation of crack curving and branching in brittle materials under dynamic loads using the extended non-ordinary state-based peridynamics. Eur J Mech A/Solids 2016;60:277–99.

[78] Bowden FP, Brunton JH, Field JE, Heyes AD. Controlled fracture of brittle solids and interruption of electrical current. Nature 1967;216(5110):38–42.

[79] Dipasquale D, Zaccariotto M, Galvanetto U. Crack propagation with adaptive grid refinement in 2D peridynamics. Int J Fract 2014;190(1-2):1–22.

[80] Belytschko T, Chen H, Xu J, Zi G. Dynamic crack propagation based on loss of hyperbolicity and a new discontinuous enrichment. Int J Numer Methods Eng 2003;58(12):1873–1905.